JGR Solid Earth

Tao Yuan and Yuankai Yang contributed equally to this work.

Key Points:
- A comprehensive study on the representative elementary volume (REV) for diffusive radionuclide transport in heterogeneous clay rocks
- Development of a method to correlate the 3D REV for diffusivity to the 2D representative elementary area for porosity via Archie's law and a characteristic length
- Validation of the predicted REV for diffusivity using data from through-diffusion experiments that confirm the general applicability of the proposed method

Supporting Information:

Supporting Information may be found in the online version of this article.

Correspondence to:

T. Yuan and Y. Yang,
tao.yuan@uni-tuebingen.de;
y.yang@fz-juelich.de

Author Contributions:
Conceptualization: Tao Yuan, Yuankai Yang
Formal analysis: Tao Yuan, Yuankai Yang, Naila Ait-Mouheb

A Comparative Study on Heterogeneity of Clay Rocks Using Pore-Scale Diffusion Simulations and Experiments

Tao Yuan[1,2] , Yuankai Yang[3] , Naila Ait-Mouheb[3], Guido Deissmann[3] , Cornelius Fischer[1] , Thorsten Stumpf[1], and Dirk Bosbach[3]

[1]Institute of Resource Ecology, Helmholtz-Zentrum Dresden-Rossendorf (HZDR), Dresden, Germany, [2]Department of Geosciences, University of Tübingen, Tübingen, Germany, [3]Institute of Energy and Climate Research, Nuclear Waste Management (IEK-6), and JARA-CSD, Forschungszentrum Jülich GmbH (FZJ), Jülich, Germany

Abstract Accurate modeling and simulation of radionuclide migration in clay rocks such as the Opalinus Clay (OPA) play a key role in the safety assessment of deep geological repositories for nuclear wastes. At the continuum scale, the representative elementary volume (REV) is a fundamental constraint to quantify the effective diffusivity, which is a key parameter in reactive transport (RT) models. Therefore, an accurate estimation of the REV is essential for a meaningful continuum-scale RT simulation in heterogeneous clay rocks. This study presents a comprehensive analysis of the heterogeneities of porosity and effective diffusivity in clay rocks by using the classical sampling theory and pore-scale simulations. First, in this study, the two-dimensional representative elementary area is correlated with the REV for porosity via a characteristic length. Next, it is shown that the REV for diffusivity is larger than the REV for porosity. Moreover, these two REVs can be correlated using Archie's law. In such a way, the REV for diffusivity can be determined by the developed correlations through analyzing two-dimensional microstructures, thus significantly reducing the computational cost. Finally, the applicability of our approach for clay rocks is validated by experimental data on the diffusion of tritiated water in the heterogeneous sandy facies of OPA. From both the experimental data and the modeling prediction, the REV for diffusivity in the sandy facies of OPA is in the order of cubic centimeters. This study provides critical insights into the diffusion in heterogeneous clay rocks toward an enhanced predictability of radionuclide migration.

Plain Language Summary Contaminant migration in clay rocks is dominated by molecular diffusion due to their low permeability. To accurately simulate this process at the centimeter scale and above, the rocks can be assumed as homogeneous media only if their volume is larger than a critical volume, also known as the representative elementary volume (REV). Therefore, an accurate estimation of this critical volume is necessary for numerical modeling of contaminant migration in clay rocks. Calculating the REV in clay rocks is a major challenge. Therefore, in this study, the REV in clay rocks was systematically investigated, and easy-to-use correlations were established for rapid estimation of REV using two-dimensional micrographs of the rocks. These critical findings contribute to a better understanding of rock microstructures and to improved calculations of contaminant migration in clay rocks.

1. Introduction

Clay rocks such as the Opalinus Clay (OPA) in Switzerland are considered as potential host rocks for deep geological disposal of nuclear wastes. Radionuclide migration in clay rocks is dominated by molecular diffusion highly dependent on the pore network geometries. In the sandy facies of OPA (SF-OPA), this pore network is critically modified due to compositional variability and owing to diagenetic reaction products, for example, carbonate and sulfide minerals (Philipp et al., 2017). Such spatial variability is responsible for heterogeneous diffusion patterns (Kulenkampff et al., 2015). At the continuum scale, the representative elementary volume (REV) is an important parameter for understanding and modeling the reactive transport (RT) of contaminants and radionuclides. An accurate estimation of the REV for diffusion is decisive for a meaningful continuum-scale simulation of radionuclide migration in heterogeneous clay rocks like SF-OPA, thus playing an important role in the safety analysis of deep geological repositories for nuclear waste.

In continuum mechanics for a heterogeneous material, the REV is the smallest volume over which a measurement can be made to produce a representative value of the macroscopic property in three-dimensional space (3D) (Bear

& Bachmat, 1984). Recently, analytical imaging techniques with different spatial resolutions were applied to provide the pore network geometries for various clay rocks (Houben et al., 2014; Keller & Holzer, 2018; Keller et al., 2013). Consequently, the REV for porosity can be easily estimated using classical sampling theory to understand the microstructural heterogeneities of the various materials (Kanit et al., 2003). By analyzing focused ion beam nano-tomography (FIB-nt) data of the pore space, Keller et al. (2013) determined that the REV for porosity in OPA is about 100^3 μm^3. In cement pastes, the REV for porosity was found to have a similar value of 100^3 μm^3, based on laser scanning confocal microscopy measurements (Yio et al., 2017). For the analysis of sandstone reservoir rocks, which have a larger grain and pore size, X-ray micro-computed tomography has been applied for the estimation of the REV for porosity (Fernandes et al., 2012). The results show that the porosity is representative of all samples with a side dimension of 1,400 μm, indicating that the REV for porosity in these sandstone reservoir rocks is about $1,400^3$ μm^3.

In two-dimensional (2D) conditions, the representative elementary area (REA) is the smallest area that can statistically represent the macroscopic property of the material. By analyzing scanning electron microscopy (SEM) data from both, the shaly and sandy facies of OPA, it was shown that the REA for the sandy facies is larger than for the shaly facies due to the coarse-grained clastic components and diagenetic carbonates in the sandy facies (Houben et al., 2014). Compared to the 3D imaging method, 2D imaging has the advantage of being widely accessible for providing information on sub-grain and intragranular variations in mineralogy (Peters, 2009; Pret et al., 2010; Robinet et al., 2015), while it cannot directly provide pore network connectivity. At a comparable resolution (2–4 μm), both 2D and 3D imaging analyses can provide relatively equivalent predictions of rock permeability based on the correspondingly resolved pore network topology (Beckingham et al., 2013). Although these studies provided detailed insights into the complexity of the microstructure of the materials concerning their porosity, the implementation of REV for porosity in continuum-scale diffusive transport processes remains questionable. As stated by Keller et al. (2013), the REV could be different for various properties indicating that the REV for porosity cannot be simply utilized for continuum-scale diffusive transport simulations. Therefore, the consistency of REVs between mineralogical composition and diffusion should be further investigated within a geostatistical framework.

To estimate the REV for diffusivity, a quantification of the effective diffusivity is a prerequisite step through both experimental and numerical methods. The diffusivity of OPA has been determined based on the analysis of mass flux and tracer activities at the outlet of diffusion cells under steady-state conditions in the laboratory (Van Loon et al., 2003, 2005) or by fitting a model to the measured tracer concentrations in boreholes under in-situ conditions (Glaus et al., 2015; Soler et al., 2015; Van Loon et al., 2004; Wersin et al., 2008). These experiments can provide the effective diffusivities of each tracer with a homogeneous diffusion assumption. Combining imaging techniques and numerical simulations, digital rock physics (DRP) provides a valuable tool to quantify the effective diffusivity of various rocks, exemplified by weathered basalts (Navarre-Sitchler et al., 2009) or cementitious materials (Yang & Wang, 2018). Recently, Yuan and Fischer (2021) proposed an integrated upscaling workflow from nm-scale to μm-scale based on multi-scale DRP to estimate the effective diffusion coefficient of radionuclides in OPA. In the upscaling workflow, the synthetic digital rocks are constructed using the stochastic reconstruction method Quartet Structure Generation Set (QSGS) (Wang et al., 2007), which has been applied to provide digital rock models of shale matrices (Chen et al., 2015) and cementitious materials (Yang & Wang, 2018; Yang et al., 2019) for permeability and diffusivity predictions, respectively.

This study aims to analyze and correlate the REVs for both porosity and effective diffusivity of clay rocks based on synthetic digital rock models using the classic sampling theory. This study first determined the REA and REV for porosity based on the 2D and 3D microstructures of synthetic clay rock, respectively, and then correlate these two parameters via a defined characteristic length using a lineal-path function (cf. steps (1–3) in Figure 1). Next, pore-scale simulations are applied to quantify the effective diffusivity in digital rocks at the micrometer scale, in which the 3D diffusion equation is numerically solved by our previously developed numerical simulators (Yang & Wang, 2018; Yuan & Qin, 2020; Yuan et al., 2019). The calculated effective diffusivities are utilized to estimate the REV for the diffusivity (cf. step (4) in Figure 1). Moreover, a robust correlation between the REV for porosity and that for diffusivity is derived and validated using two case studies with different microstructures (cf. step (5) in Figure 1). Following this developed method, the REV for effective diffusivity can be estimated based on the 2D microstructure of the clay rocks, thus significantly reducing the computational cost. Finally, our developed method is validated against data from tritiated water (HTO) through-diffusion experiments performed in SF-OPA.
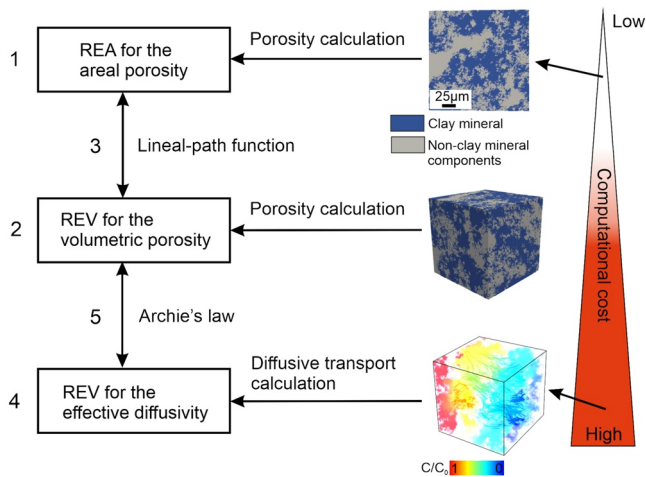
Figure 1. Schematic overview of the proposed workflow of representative elementary volume (REV) and representative elementary area (REA) analysis. This includes REV quantification for porosity (1) and diffusivity (2) based on porosity and diffusion transport calculations, respectively, the correlation between two REVs via Archie's law (3), the determination of REA for porosity based on 2D microstructure analysis (4), and correlation between REA for porosity and REV for porosity via the lineal-path function (5). Using the proposed workflow, the REV for diffusivity (step 2) can be obtained from REA for porosity (step 4) with significantly reduced computational cost.

2. Methodology

2.1. REV and REA Determination

The REVs for porosity and effective diffusivity and the REA for porosity were determined using the classical sample theory (Kanit et al., 2003) as shown in Figure 2. For this, the first 10 different synthetic microstructures of shale with a size of 800^3 μm^3 were constructed (cf. step (a) in Figure 2). For each microstructure, various sub-regions with five different volumes of 800^3, 400^3, 200^3, 100^3, 50^3, and 25^3 μm^3 were extracted. For each volume, one sub-region was randomly selected within one microstructure, resulting in 10 different sub-regions per volume among the 10 microstructures (cf. step (b) in Figure 2). To obtain the 2D microstructure, we randomly extracted one cross-sectional surface for each sub-region, resulting in 50 different 2D microstructures. For each subset, the porosity and the effective diffusivity were quantified (see Section 2.3 for a detailed description of the quantification of diffusivity). As the last step, a geostatistical analysis was performed to estimate the REVs for porosity and diffusivity.

Based on classical sampling theory, the relative error on the exact mean value of a given property M_D is defined as

$$\varepsilon(l) = \frac{2\sigma_D(l)}{M_D}, \tag{1}$$

where σ_D is the standard deviation of the property for the cubic subsets with the identical edge length of l. The REV for the given property can be determined with a predefined relative error. Considering that the uncertainties of our experimental measurements are mostly over 5%, this study employed 10% as the predefined relative error, $\varepsilon = 10\%$, which was also used in many previous studies (Houben et al., 2014; Keller et al., 2013).

2.2. Digital Rock Reconstruction

The sandy facies of OPA shows a heterogeneous microstructure with distinguishable sandy layers and diagenetic carbonate lenses (Houben et al., 2014; Philipp et al., 2017). In this study, the two-scale QSGS method based on stochastic clustering growth theory is utilized to generate the digital rocks approximating the heterogeneous microstructures of shale rocks (Wang et al., 2016). The original QSGS includes four controlling parameters to randomly reconstruct the pore geometry of a porous medium, enabling regenerated microstructures to maintain the same statistical features as the real porous medium, for example, with respect to porosity (Wang et al., 2007). Compared with the original QSGS, this modified QSGS method can generate a heterogeneous structure by combining coarse and refined structures by introducing two different core distribution probabilities, c_f, c_d, and
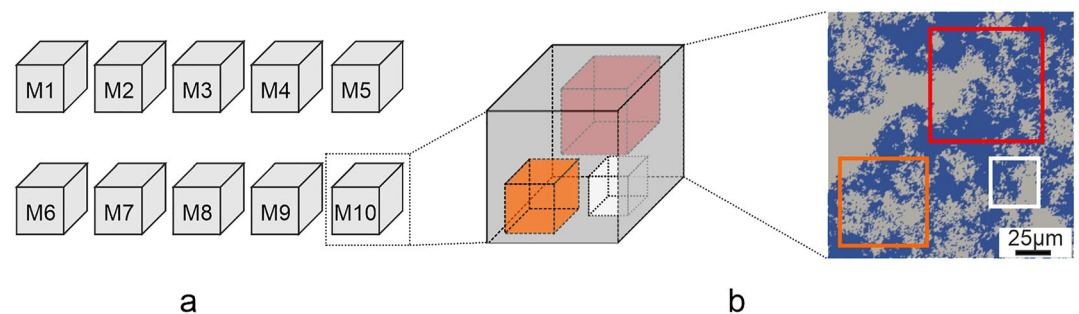
Figure 2. Schematic representation of the reconstruction of 10 microstructures (M1–M10) of the shale (a), and extraction of various sub-regions with different volumes (b). The volumes of the microstructures and extracted sub-regions are 800^3, 400^3, 200^3, 100^3, 50^3, and 25^3 μm^3, respectively. For each volume, one sub-region is randomly extracted within the entire domain (e.g., red, orange, and white squares represent three randomly selected sub-regions with different volumes).

a
b

Figure 3. Schematic representation of heterogeneous microstructures of clay rocks including clay mineral aggregates (blue color) and non-clay mineral grains (gray color). The digital rock models are partitioned into a mesh of 200×200 grids with a pixel size of 1 μm. The controlling parameters in two-scale Quartet Structure Generation Set for structures (a) S1 and (b) S2 are listed in Table 1.
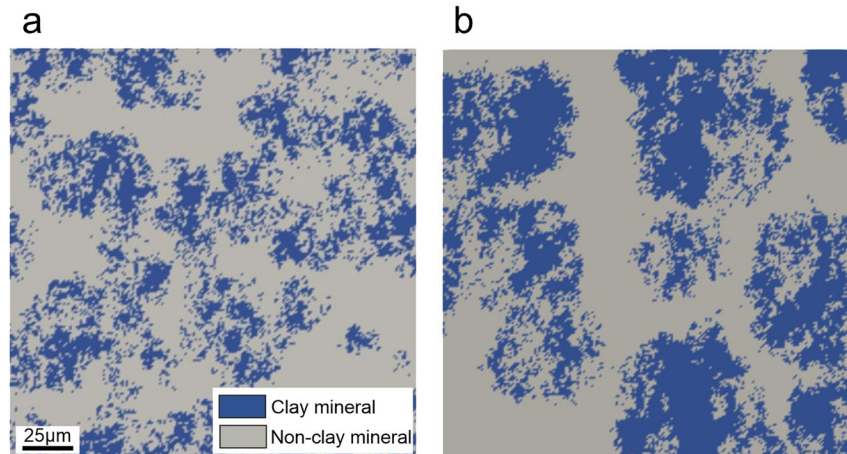
volume fractions ε_c, ε_f (Wang et al., 2016). The final volume fraction of the clay minerals is $\phi_c = \varepsilon_c \times (1 - \varepsilon_f)$. Figure 3 shows cross-sections of two heterogeneous microstructures (S1 and S2) generated with different parameters that are listed in Table 1. The digital rocks in Figures 3a and 3b contain 30% and 44% clay minerals, respectively, thus having similar volume fractions of clay minerals as the mixture of clay and sandy laminae of SF-OPA (Bossart & Thurry, 2008). For a more detailed algorithm of the modified QSGS method and descriptions of controlling parameters, the readers are referred to Text S1 in Supporting Information S1. Based on the FIB-SEM and mercury intrusion porosimetry (MIP) analyses in a previous study (Bollermann et al., 2022), pores with throat diameters between 8 and 60 nm in the clay-dominated subfacies of OPA contribute the most to the total porosity (90%). Moreover, at the micrometer scale, the microstructure of SF-OPA investigated, for example, by SEM images reveals calcite and quartz as the major non-clay constituents, which are considered as impermeable, based on FIB/Broad Ion Beam (BIB) imaging data (Keller & Holzer, 2018; Keller et al., 2013; Philipp et al., 2017). By utilizing chemical element mapping analyses acquired by SEM (Pret et al., 2010) and ³H-polymethyl methacrylate (PMMA) autoradiographic technique (Robinet et al., 2015), the 2-D porosity mappings of clay rocks were obtained. Based on the measured data, they found the porosities in non-clay constituents (i.e., carbonates) were comparatively low (e.g., $\phi_{calcite} = 5\%$ in Pret et al. (2010) and $\phi_{calcite} < 4\%$ in Robinet et al. (2015)). Consequently, the non-clay constituents were treated as impermeable. Therefore, in this study, we consider the clay minerals as the only porous phase and non-clay constituents as non-porous phase. Further, we assumed that the clay mineral phase has a homogeneous porosity (Keller et al., 2015) and considered the various mineral distributions in the microstructures to characterize the heterogeneous porosity distribution in OPA. Therefore, the porosity ϕ is correlated to the volume fraction of the clay minerals ϕ_c as $\phi = \alpha_c \cdot \phi_c$ (Keller et al., 2015), where α_c is the porosity of clay minerals.

2.3. Quantification of Effective Diffusivity

The effective diffusion coefficients of the clay rocks were determined using pore-scale simulations based on synthetic multiscale digital rock models (Yang et al., 2019; Yuan & Fischer, 2021). At the micrometer scale, the diffusion-sorption equation is used to describe the diffusive transport of a solute in the porous media, written as follows:

$$\frac{\partial C_{tot}}{\partial t} + \nabla \cdot \boldsymbol{J} = 0, \tag{2}$$

Table 1
Controlling Parameters Used for the Digital Rocks Reconstructed by the Two-Scale Quartet Structure Generation Set Method, and the Corresponding Characteristic Lengths R_c

Set No.	c_d	c_f	ε_c	ε_f	ϕ_c	R_c (μm)
S1	5.0×10^{-5}	2.0×10^{-3}	0.60	0.15	0.30	16.4
S2	5.0×10^{-6}	1.0×10^{-4}	0.65	0.27	0.44	23.8
S3	5.0×10^{-6}	1.0×10^{-4}	0.90	0.07	0.84	10.8
S4	5.0×10^{-6}	1.0×10^{-4}	0.85	0.11	0.57	21.0
S5	1.5×10^{-5}	5.0×10^{-5}	0.85	0.11	0.68	17.5
S6	1.0×10^{-5}	1.2×10^{-4}	0.70	0.15	0.45	23[a]

[a]Predicted by the normalized lineal-path function in Section 2.4.

where C_{tot} is the total concentration of an aqueous solute defined as $C_{tot} = \alpha C$, where C is the concentration of the aqueous solute at the micrometer scale, and J is the flux through the entire domain. Assuming a linear sorption isotherm with a distribution coefficient K_d (Leupin et al., 2017; Wersin et al., 2008), the constant rock capacity factor α can be calculated by $\alpha = \phi + \rho_{bd} K_d$ with the porosity ϕ and the bulk dry density ρ_{bd}. Constant concentration conditions are used at the inlet and outlet $C_{tot} = C_{in}$ or C_{out}. We assume for simplicity that the clay rocks (i.e., here sandy OPA) are composed of permeable clay minerals and impermeable non-clay mineral components including quartz, calcite, and pyrite (Bossart & Thurry, 2008; Keller & Holzer, 2018; Keller et al., 2015). Therefore, the diffusion is controlled by the geometry of the clay mineral aggregates as well as the diffusivity through the clay matrix at this scale. In this study, we assume that the clay matrix has a homogeneous diffusivity. The diffusive flux is then calculated by:

$$J = \begin{cases} -D_e^{\text{clay}} \nabla C, & \text{in the clay mineral aggregates} \\ 0, & \text{in the non} - \text{clay mineral components} \end{cases}. \tag{3}$$

The 3D Equations 2 and 3 are numerically solved by a previously developed numerical simulator using the supercomputer JURECA-DC at Forschungszentrum Jülich (Jülich Supercomputing Centre, 2018; Yuan & Qin, 2020; Yuan et al., 2019). The effective diffusion coefficient of the digital rock at the micrometer scale is finally estimated by the total mass flux J per unit cross-sectional area under steady-state conditions:

$$D_e = \frac{J \cdot L}{(C_{in} - C_{out})}, \tag{4}$$

where L is the length of the domain. For more details on the numerical solution strategies and their validations, the readers are referred to Yang et al. (2019) and Yuan and Fischer (2021).

2.4. Characteristic Length to Link REV and REA for Porosity

In this section, we propose a characteristic length to correlate the REV for porosity (REVϕ) with the REA for porosity (REAϕ). Thus, the REV for porosity can be determined by the analysis of the 2D microstructure of the clay rocks (determined, e.g., by the analysis of SEM data). In this study, we assume for simplicity that clay rock is a two-phase material consisting of clay minerals and non-clay minerals. As an important morphological descriptor to statistically measure the structure of random media, the lineal-path function $L^j(r)$ describes the probability that a line segment of length r lies entirely in phase j ($j = 1, 2$) (Yeong & Torquato, 1998). This function contains connectedness information about phase j, at least along a lineal path of length r, where $L^j(0)$ is equal to the volume fraction of phase j, ϕ_j (Hornung, 1997; Lu & Torquato, 1992). Thus, the lineal-path function can be utilized to correlate the volumetric information with areal information via connectedness. The lineal-path function is expressed as follows (Yeong & Torquato, 1998):

$$L^j(r) = \overline{P_j(\vec{r}_1, \vec{r}_2)}, \text{ and } P_j(\vec{r}_1, \vec{r}_2) = \begin{cases} 1, & \text{when } \forall \vec{r}_x \in v_j \\ 0, & \text{otherwise} \end{cases}, \tag{5}$$

where $\overline{}$ denotes the mean value, $\vec{r}_1, \vec{r}_2$ are any two points in the porous medium with a distance r, $\vec{r}_x$ is the point on the straight line connecting points $\vec{r}_1$ and $\vec{r}_2$ ($\vec{r}_x \in [\vec{r}_1, \vec{r}_2]$) and v_j is the subset occupied by phase j.

Here, we define the normalized lineal-path function as $L_N^j(r) = L^j(r)/\phi_j$, which follows $L_N^j(0) = 1$ and $L_N^j(\infty) = 0$. To calculate $L_N^j(r)$ for a heterogeneous polydispersed-sphere medium, Lu and Torquato (1992) developed an approximate formula, which was expressed as:

$$L_N^j(r) = \exp\left[-m \frac{(1 - \phi_j) r}{\phi_j R_{c,j}}\right], \tag{6}$$

where $R_{c,j}$ is the characteristic length for phase j and m relates to the size distribution of polydispersed spheres. Based on the definition of $L^j(r)$, $R_{c,j}$ represents an average distance over which a linearly moving point inside
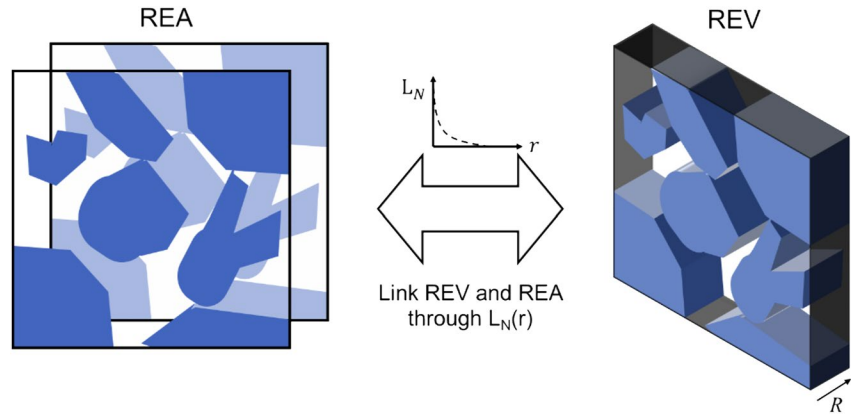
Figure 4. Schematic representation of a characteristic length R to correlate the representative elementary volume ϕ with the representative elementary area ϕ. An identical area fraction of clay minerals (blue color) is assumed when the surface is inside of two surfaces with a distance of R.

phase j reaches its phase boundaries. It indicates that any two points will be statistically located in the same phase, when their spatial distance is equal to or less than $R_{c,j}$. Therefore, we assume that two parallel sections of a microstructure with a distance less than R_j have an identical area fraction of phase j. As previously mentioned in Section 2.1, $\varepsilon(l)$, $\varepsilon(S)$, and $\varepsilon(V)$ are the relative errors as a function of the edge length, area, and volume of extracted cubic sub-regions, respectively. By using the assumption above, the relative error of the volumetric phase fraction as a function of volume $\varepsilon_V(V)$ can be linked to the relative error of the area phase fraction with area $\varepsilon_A(S)$ through $R_{c,j}$: $\varepsilon_V(V) = \varepsilon_A(S)$, as $V = S \times R_c$. Here, a relative error of the area phase fraction as a function of volume is defined as: $\varepsilon_{VA}(V)$. With $V = S \times R_c$, we can identify $\varepsilon_{VA}(V) = \varepsilon_A(S)$. By assuming that only the clay mineral aggregates are considered as permeable, one can get:

$$\varepsilon_V(V) = \varepsilon_\phi(V). \tag{7}$$

Finally, we get the following equation:

$$\varepsilon_\phi(V) = \varepsilon_V(V) = \varepsilon_{VA}(V) = \varepsilon_A(S). \tag{8}$$

Consequently, as illustrated in Figure 4, the REV can be correlated with REA via R_c if setting an identical predefined relative error:

$$\text{REV} = \text{REA} \times R_c. \tag{9}$$

Note that REV and REA discussed above are accounted for volume and area phase fractions, respectively. After calculating the phase fractions of the volume and area and the lineal-path functions of several generated microstructures, R_c and m can be determined by using global optimization. The parameter m is the same for all microstructures while the parameter R_c has a different value for each one.

2.5. Correlation Between REVs for Porosity and Diffusivity

In this section, a mathematical equation to correlate the REVs for porosity and diffusivity is presented. In current diffusion studies, the effective diffusivity is usually correlated with the total porosity (ϕ) and the diffusion coefficient of a tracer in free water (D_0) via Archie's law (Appelo et al., 2010; Boving & Grathwohl, 2001; Grathwohl, 1998):

$$D_e = a D_0 \phi^n, \tag{10}$$

where n and a are empirical coefficients. Taking the logarithmic functions on both sides of Equation 10 leads to: $\ln(D_e/D_0) = n \ln \phi + \ln(a)$. As described in Section 2.1, the REV for a given property can be determined with a

predefined relative error, which is calculated by the standard deviation of the property (cf. Equation 1). Therefore, the standard deviations of $\ln(D_e/D_0)$ and $\ln \phi$ have the following mathematical relationship:

$$SD(\ln(D_e/D_0)) = n \times SD(\ln \phi), \tag{11}$$

where SD denotes the operation of standard deviation.

Note that pore connectivity is another important factor affecting the transport properties of rocks, such as diffusivity and permeability (Bernabé et al., 2016). The pore connectivity can be characterized by the mean coordination number in the pore network models (Bernabé et al., 2010, 2011). Usually, the total porosity in clay rocks contains isolated and dead-end pores, which have a negligible contribution to transport processes (Oh & Jang, 2004). Nevertheless, the total porosity is easier to be measured and calculated than the pore connectivity in clay rocks. Therefore, the effective diffusivity is usually correlated to the total porosity using Archie's law (Appelo et al., 2010; Grathwohl, 1998).

Based on the mathematical calculation (dos Santos & Menon Junior, 2020; Kim et al., 2017), the relative errors of porosity and effective diffusivity can be correlated through n (see Text S2 in Supporting Information S1 for a detailed derivation):

$$n \times \varepsilon_V = n \times \varepsilon_\phi = \varepsilon_{D_e/D_0}. \tag{12}$$

Consequently, we can predict the value of ε_{D_e/D_0} through ε_ϕ. As described in Section 2.1, the REV for a given property can be determined as $\varepsilon = 0.1$. Therefore, the REV for effective diffusivity can be quantified with a predefined value of $\varepsilon_{D_e/D_0} = 0.1$, which is equivalent to $\varepsilon_\phi = 0.1/n$ based on Equation 12. To validate Equation 11, we first select the calculated effective diffusivities and porosities of sub-regions with volumes of $400^3 \ \mu m^3$. The empirical exponent n in Archie's law can then be determined by analyzing the calculated two properties. Next, with the same data set, the standard deviations of $\ln(D_e/D_0)$ and $\ln \phi$ are analyzed and correlated. Finally, the comparison between the empirical exponent coefficient n in Archie's equation and the slope of the linear correlation between the standard deviations of $\ln(D_e/D_0)$ and $\ln \phi$ will be utilized to validate Equation 11.

Note that the main objective of this study is to present an approach to correlate the 3D REV for diffusivity and the 2D REA for porosity. Archie's law might not be applied to correlate porosity and diffusivity for charged ions due to surface diffusion in the diffuse layer of the clay surface (Glaus et al., 2007). Moreover, small pores in non-clay minerals play an important role in transport processes in argillaceous rocks with a low clay mineral content (<10%–15%) (Robinet et al., 2012). Consequently, Archie's law might not be appropriate to correlate porosity and diffusivity at low clay mineral content. Alternatively, other correlations (e.g., Koponen's equation) have been utilized to improve the fitting of the model to the calculated data (Robinet et al., 2012). Nevertheless, as a starting point, we focus on neutral species (e.g., HTO). Thus Archie's law can be applied as a first approximation to correlate porosity and diffusivity (Cosenza et al., 2021).

2.6. Through-Diffusion Experiments in Sandy Facies of Opalinus Clay

The applicability of the methodology described above was validated by through-diffusion experiments in samples from the sandy facies of OPA using HTO. The samples were taken from a drill core extracted from borehole BAD oriented parallel to the bedding of SF-OPA from the Mont Terri underground rock laboratory in Switzerland. To avoid any contamination from the drilling process, three samples (labeled BAD-1, BAD-2, and BAD-3) representative of the heterogeneity of the drill core (cf. Figure 5) were taken from the center of the core, after removing the outer 2 cm using a diamond saw. The samples consist of different proportions of darker gray clay layers, containing inter alia illite, illite/smectite mixed layers, kaolinite and chlorite, and yellowish-brownish sandy layers, made up predominantly of quartz and carbonates (mainly calcite) with a generally layered texture. The through-diffusion experiments parallel to the bedding were conducted with a cylindrical diffusion cell to derive the HTO transport parameters. The neutral tracer HTO was chosen to determine the total connected transport porosity since it is assumed that neutral species can diffuse through all pore spaces.

In the experimental setup, cylindrical clay samples (thickness: 10 ± 0.1 mm; cross-sectional area: 707 ± 10 mm^2) were embedded in an epoxy resin (Epofix, Struers GmbH) which formed a sample holder. The cylindrical clay sample was mounted in the PMMA cylinder creating on one side the "high concentration reservoir" and on the other side the "low concentration reservoir." The total volumes of the high and low concentration reservoirs
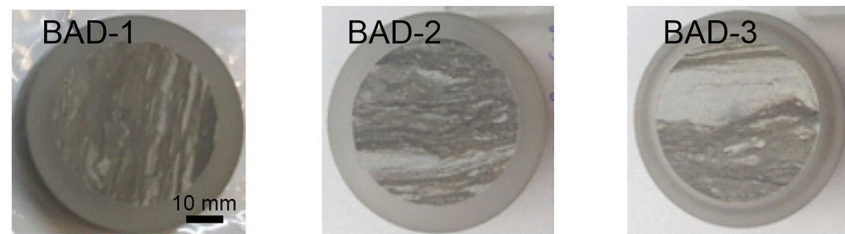
Figure 5. Photographs of the three heterogeneous drill core samples (BAD1–BAD3) used in the tritiated water-through diffusion experiments. Dark gray: clay-rich layers, light gray: sandy layers containing quartz and carbonates (mainly calcite) in different proportions.

were 500 and 25 mL, respectively. The rock samples were sandwiched between sintered titanium filters (Mott Corporation, Germany) with a porosity of 0.1, a diameter of 0.038 m, a thickness of 0.001 m, and a pore diameter of 1×10^{-5} m. A multi-channel peristaltic pump (Watson Marlow, United Kingdom) circulated the pore solution through the tubing system toward the sample. Before the through-diffusion experiments were started, each sample was saturated with tracer-free clay pore water (Pearson, 1998) by adding the respective solution to the high and low concentration reservoir and leaving it in contact with the clay sample for 5 weeks. To initiate the diffusion, the solution inside the high concentration reservoir was spiked with HTO and a concentration gradient was maintained with a concentration of $1.86 \cdot 10^{-9}$ M in the upstream compartment (see Figure S1 in Supporting Information S1) and zero concentration in the downstream compartment. The accumulated activity was determined in the low concentration reservoir by measuring the activity (in Bq) of HTO in the solution by liquid scintillation counting (Quantulus, PerkinElmer) as a function of time. The diffusive flux was calculated according to the method of Van Loon et al. (2003).

3. Results and Discussion

Six sets of microstructures (S1–S6) were constructed by using the two-scale QSGS method (cf. Section 2.2) with the controlling parameters listed in Table 1. For each set of microstructures, 10 structures were randomly generated by using the same parameters, resulting in 60 different microstructures. These reconstructed microstructures are utilized to determine and validate the parameters of the proposed correlations. In the first step, the REA for porosity is correlated with the REV for porosity. The optimized lineal-path functions were obtained to determine the characteristic length for the correlation (cf. Section 3.1). Because the microstructures of S1 and S2 have a similar volume fraction of clay minerals as the mixture of clay and sandy laminae of SF-OPA (cf. Section 2.2) and the development of correlation between REVs for porosity and diffusivity does not need the global optimization utilized in Section 3.1. Therefore, the microstructures of S1 and S2 are used in Section 3.2 for analyzing the REVs for porosity and diffusivity and developing the correlation between the two REVs. At last, the proposed correlations applied in clay rocks are validated using the experimental data from SF-OPA (Section 3.3).

3.1. Correlation Between REA and REV for Porosity

Figure 6. Relative errors of areal porosity (black and gray lines and dots) $\varepsilon_A(l)$ and volumetric porosity (red line and dots) $\varepsilon_V(l)$ versus the side length for microstructure S1. Method 1 represents the randomly extracted subsets. Method 2 represents the extraction method with a fixed center of subsets. The relative error of areal porosity with method two is smaller than with method 1 due to the larger overlapping area of subsets, resulting in a smaller representative elementary area.

Figure 6 illustrates the relative errors of porosity for the 2D and 3D microstructures of S1 as a function of the edge length of the subset, which shows a linear correlation on a log-log scale. Both relative errors decrease with increasing edge length due to more statistically representative properties with a larger length. From Figure 6, the relative error for the volumetric porosity is smaller than that for the areal porosity, which indicates the length for volumetric porosity is smaller than that for areal porosity with a same relative error. With a suggested relative error of 10%, the length of the REA for porosity is about 328 μm, which has a good agreement with the estimated
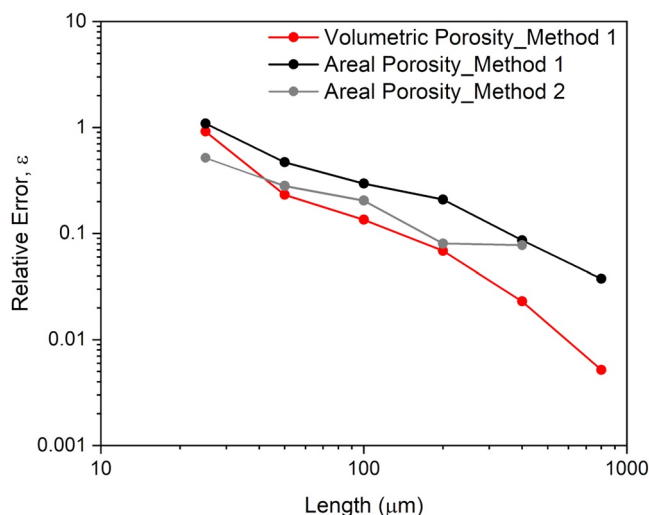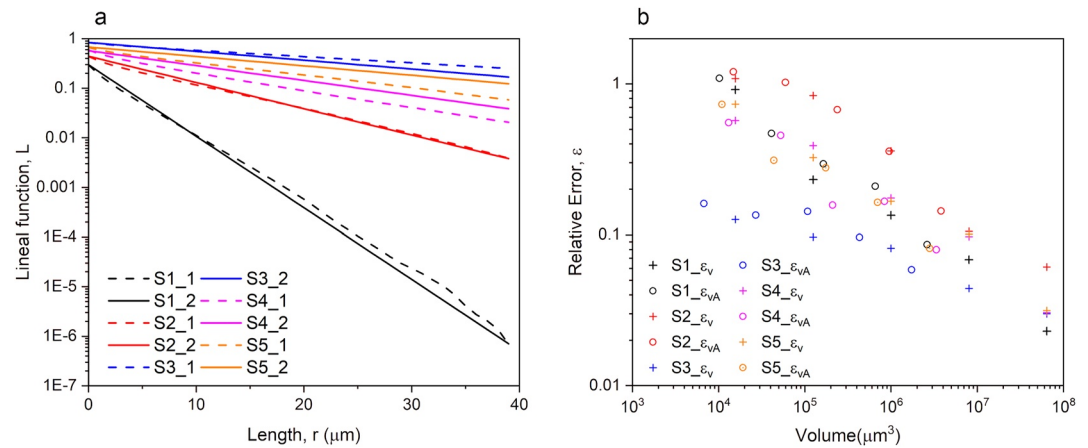
Figure 7. (a) Lineal-path functions $L^c(r)$ of clay minerals versus the distance r for microstructures S1–S5. Colored dashed lines denote the results that are determined by Equation 5 based on the corresponding microstructures; colored solid lines denote the results that are fitted based on Equation 6 with $m = 2.3$. (b) Comparison of the relative error of the volumetric porosity $\varepsilon_V(V)$ (colored crosses) and $\varepsilon_{VA}(V)$ (colored open circles) (cf. Equation 8) for microstructures S1–S5. The corresponding characteristic lengths R_C for the correlations are listed in Table 1. The good agreements between $\varepsilon_V(V)$ and $\varepsilon_{VA}(V)$ for each case demonstrates the robust correlations between representative elementary area and representative elementary volume for porosity.

value for Callovo-Oxfordian claystone by Cosenza et al. (2019). Houben et al. (2014) reported that the length of the REA for porosity in a mixture of clay and sand layers in SF-OPA is about 245 ± 10 μm, based on the quantitative analysis of mineralogy and porosity acquired by BIB-SEM image data. In Houben et al. (2014), the center of the different subsets was fixed at the same point, resulting in an increased overlapping area with increasing edge length. Consequently, the porosities among the different subsets are statistically relevant. In our study, subsets were selected randomly with different lengths to minimize the effect of overlapping to improve the statistics in the determination of the representative value. Therefore, the relative error for areal porosity is larger than the one calculated using the previous extraction method with a fixed center of subsets (Figure 6).

To develop the correlation between REA and REV for porosity, the unknown parameters, m and R_c are first determined using global optimization (multiparameter nonlinear fitting method) based on the microstructures S1–S5. To determine the values of m and $R_{c,j}$ in Equation 6 for microstructures S1–S5, the objective of optimization in this work is to find the minimum of the sum of the difference between the lineal-path function values predicted by Equation 6 and the calculated values based on the microstructures, as well as the difference of the two curves of $\varepsilon_V(V)$ and $\varepsilon_{VA}(V)$. Hence, for each microstructure, first the lineal-path functions $L^c(r)$ of the clay minerals versus the distance r are calculated using Equation 5, and the relative error functions $\varepsilon_V(V)$ and $\varepsilon_A(S)$ are determined. Through the global optimization, the parameter m equals 2.3; the values of R_c for each microstructure are summarized in Table 1. Figure 7a illustrates the lineal-path functions L for the microstructures S1–S5 (colored dashed lines) in comparison to the fitted curves (colored solid lines) using Equation 6 with $m = 2.3$ and the corresponding R_c values listed in Table 1. As expected, the lineal-path functions decrease exponentially with increasing the measured distance r. Figure 7b illustrates the comparison between $\varepsilon_V(V)$ (colored crosses) and correlated $\varepsilon_{VA}(V)$ using R_c (colored open circles) as a function of measured volumes for microstructures S1–S5. The good agreement between the two values demonstrates that the proposed method (i.e., Equation 6 with $m = 2.3$) can be utilized to correlate REA and REV regarding the porosity. Next, we utilize the microstructure S6 to validate the proposed method. As illustrated in Figure 8a, $R_c = 23$ μm can be obtained by fitting the lineal-path function values calculated by Equation 6 with $m = 2.3$ (dashed line) to the values based on the microstructures (solid line). In Figure 8b, the two curves of relative errors $\varepsilon_V(V)$ and $\varepsilon_{VA}(V)$ versus the measured volume show a good agreement using $R_c = 23$ μm without direct fitting, which indicates the accuracy and robustness of the developed method.
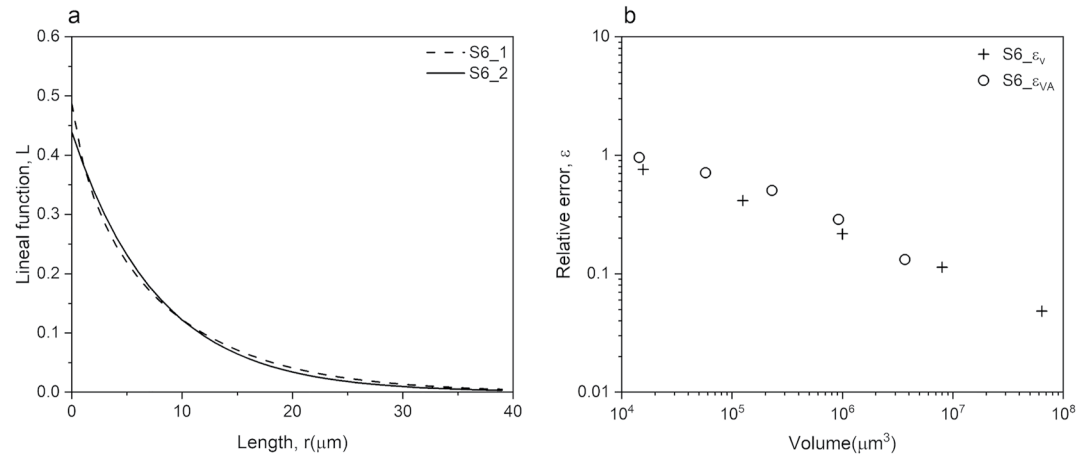
Figure 8. (a) Lineal-path function $L^c(r)$ of the clay minerals versus the distance r based on the microstructure S6 (dashed line) and lineal-path function as a function of distance r based on Equation (6) with $m = 2.3$ and $R_c = 23\ \mu$m (solid line). Here, $m = 2.3$ is obtained from global optimization and $R_c = 23\ \mu$m is obtained by fitting the solid line to the dashed line. (b) Comparison of relative errors $\varepsilon_V(V)$ (crosses) and $\varepsilon_{VA}(V)$ (open circles) versus the measured volume for microstructure S6. The agreement between $\varepsilon_V(V)$ and $\varepsilon_{VA}(V)$ indicates that the representative elementary area is correlated with representative elementary volume via a characteristic length R_c of 23 μm.

3.2. Correlation Between REV for Porosity and REV for Diffusivity

The REVs for porosity and diffusivity in clay rocks are determined here using the proposed workflow shown in Figure 1. Here, the microstructure S1 is used as an example. The mean values and variances of the volume fraction of clay minerals and the effective diffusivity as a function of the volume of the sub-regions are shown in Figure 9a. Since the porosity is assumed to correlate to the volume fraction of clay minerals, it can be seen that the local porosity and the effective diffusivity change within different sub-regions of the microstructure due to structural heterogeneity and dispersion. The errors of the parameters decrease with increasing the volume of the sub-regions. As shown in Figure 9a, with increasing the volume size, the mean volume fraction of clay minerals
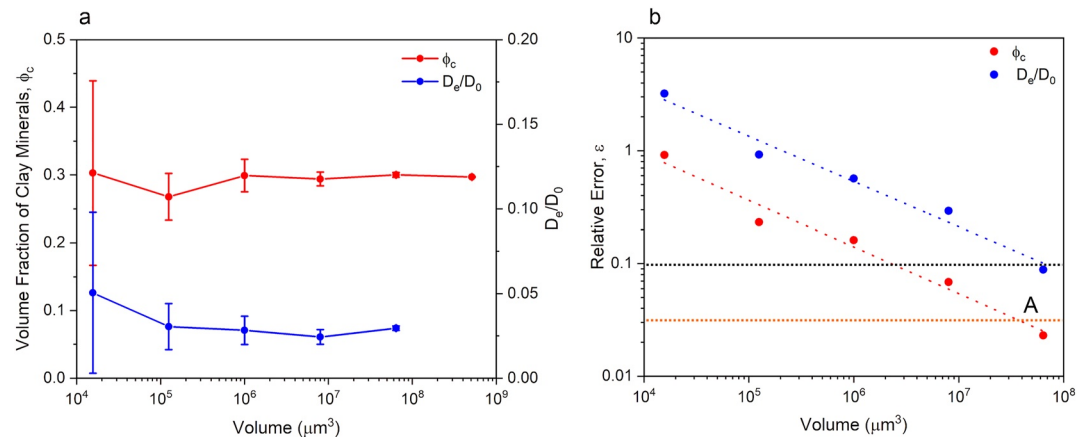

Figure 9. (a) Mean values and intervals of confidence on the mean value for the volume fraction of clay minerals (red color) and effective diffusivity (blue color) as a function of the volume of the sub-region of microstructure S1. (b) Relative errors of volume fraction of clay minerals (red dots) and effective diffusivity (blue dots) versus the volume of the sub-region. The red and blue dashed lines represent the calibration curves for the volume fraction of clay minerals and diffusivity, revealing linear trends with coefficients of determination of $R^2 = 0.97$ and $R^2 = 0.98$ on a log-log scale, respectively. The black dashed line denotes the value of $\varepsilon = 0.1$ that is used to quantify the representative elementary volume for the volume fraction of clay minerals and diffusivity based on the red and blue dashed lines, respectively. The orange dashed line represents the value of $\varepsilon/n = 0.031$, where $n = 3.18$ based on the correlation between the volume fraction of clay minerals and diffusivity for microstructure S1 (cf. Figure 10a). The intersection of the red and orange dashed lines is point A, which is used to quantify the representative elementary volume for diffusivity via the relative errors of porosity (cf. Equation 12).
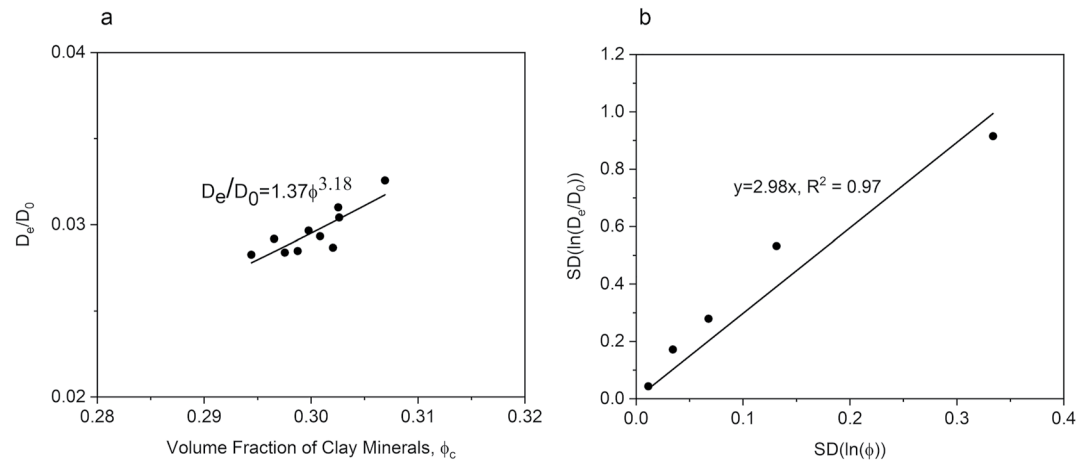
Figure 10. (a) Scatter plot of calculated effective diffusivity versus volume fraction of clay minerals in microstructure S1 (data are selected from sub-regions with a volume of 400^3 μm^3). The calculated diffusivities can be correlated to the porosity via Archie's law with an exponent of 3.18 (black line, $R^2 = 0.71$). (b) Scale plot of the standard deviation of $\ln(D_e/D_0)$ versus the standard deviation of $\ln(\phi)$. The standard deviation of $\ln(D_e/D_0)$ is linearly correlated with the standard deviation of $\ln(\phi)$ with a slope of 2.98 (black line, $R^2 = 0.97$). The same calculations for microstructure S2 are presented in Figure S3 in Supporting Information S1.

converges to a certain value (Kanit et al., 2003; Keller et al., 2013), which is referred to as the mean value of clay fraction for the whole domain (Cosenza et al., 2019). In contrast, the mean values of the effective diffusivity depend on the volume size, which reveals the different convergent trends of mean values between the porosity and other rock properties such as apparent moduli (Kanit et al., 2003) and effective diffusivity in this study.

Figure 9b illustrates the calculated relative errors of volume fraction of clay minerals and effective diffusivity as a function of the volume of the sub-region, showing a linear correlation on a log-log scale ($R^2 = 0.97$ for porosity, $R^2 = 0.98$ for diffusivity). As expected, the relative errors of both properties decrease with increasing volume because the measured properties become more statistically representative with a larger volume. With a suggested relative error of 10% (cf. black dashed line in Figure 9b) (Houben et al., 2014; Keller et al., 2013), the REV for porosity is about 131^3 μm^3 and the REV for diffusivity is about 401^3 μm^3. The significantly different REVs for porosity and diffusivity suggest that the REV for diffusivity instead of the REV for porosity should be utilized for 3D numerical modeling of the diffusive transport of solutes and radionuclides at the continuum scale.

In Bollermann et al. (2022) and Yuan and Fischer (2022), both the pores in grain-supported clay material between larger non-clay grains and intragranular pores in diagenetic calcite crystals contribute to the connective pathways for transport. We thus performed a sensitivity analysis to evaluate the effect of various effective diffusivities of the non-clay minerals $D_{e_{nonclay}}$ on the calculated relative errors of the diffusivity in clay rocks. Figure S2 in Supporting Information S1 illustrates that an increase in the $D_{e_{nonclay}}/D_{e_{clay}}$ ratio causes a decrease of the relative error for the diffusivity of the clay rocks, resulting in a smaller REV for diffusivity based on an identical predefined error. Bollermann et al. (2022) and Yuan and Fischer (2022) showed that the diffusivity in non-clay minerals is up to two orders of magnitude lower than that in clay minerals. Therefore, in this study, we assumed that the non-clay minerals are impermeable and set the diffusivity of non-clay minerals $D_{noncaly}$ equal to 0.

The calculated diffusivities of the sub-regions with a volume of 400^3 μm^3 versus the corresponding volume fraction of clay minerals are shown in Figure 10a. The calculated diffusivities of these sub-regions can be correlated to the volume fraction of clay minerals via Archie's law with an exponent of 3.18 (Figure 10a). The standard deviation of $\ln(D_e/D_0)$ versus standard deviation of $\ln(\phi)$ is shown in Figure 10b, which shows a clear linear correlation with a slope of 2.98 ($R^2 = 0.97$, cf. Equation 11). The same calculations were performed for microstructure S2 to validate the proposed correlation of Equation 11 (See Figure S3 in Supporting Information S1). Good agreements between the slope and exponent for both microstructures S1 and S2 validate the developed correlation between REV for porosity and REV for diffusivity (cf. Equations 10 and 11 in Section 2.5). As discussed above, the REV for diffusivity is about 401^3 μm^3 based on a relative error of diffusivity of 0.1 (cf. black dashed line in Figure 9b). With the determined value of $n = 3.18$, the REV for diffusivity is predicted as

Table 2
Transport Parameters Obtained by the Transport Model in COMSOL to Fit the Flux Data of Our Diffusion Experiment for Three Sandy Facies of OPA Samples From Mt. Terri, Switzerland, Tabulated in Table S1 in Supporting Information S1

Sample	$\alpha = \Phi$ [−]	Relative error	$D_e \cdot 10^{-11}$ [m²/s]	Relative error
BAD-1	0.20 ± 0.04		9.0 ± 0.2	
BAD-2	0.19 ± 0.04	0.164	8.5 ± 0.1	0.226
BAD-3	0.17 ± 0.02		7.2 ± 0.2	

324.5^3 μm³, based on a relative error of porosity with of $\varepsilon_\phi = 0.1/3.18$ (cf. orange dashed line and point A in Figure 9b). The good agreement between the REV for the diffusivity from the simulated diffusivities and the developed correlation (cf. Equation 12) shows that our proposed correlation (cf. Equation 12 in Section 2.5) can predict the REV for diffusivity based on the microstructures of clay rocks. Consequently, the computational cost can be significantly reduced without the numerical calculation of the diffusivities.

3.3. Validation of the Proposed Method by Through-Diffusion Experiments

The methodology described above was validated using experimental data from HTO through-diffusion experiments using samples from the sandy OPA facies. The diffusive fluxes of HTO and the accumulated activity data are given in Table S1 in Supporting Information S1. The transport parameters (effective diffusion coefficient D_e and accessible porosity ε_{acc}) were determined by using the numerical simulator COMSOL Multiphysics®5.5 (COMSOL AB, Stockholm, Sweden, see details in Text S3 in Supporting Information S1) and inverse modeling of the experimental data. For a neutral (conservative) tracer such as HTO, the adsorption on mineral surfaces is negligible during the diffusion processes in clay rocks (Joseph et al., 2013; Wigger & Van Loon, 2018). Therefore, the rock capacity factor α is reduced to the accessible porosity Φ of the SF-OPA samples (i.e., $K_d = 0$). A default value of K_d (HTO) of zero was proposed by Van Loon & Jakob, 2005. However, here the adsorption of HTO on clay minerals (e.g., by isotopic exchange) was accounted for by a low but non-zero K_d value of the order of 10^{-5} m³/kg, in order to reproduce the diffusion data with acceptable accuracy. The data of porosity and effective diffusivity were obtained from the transport model in COMSOL to fit the flux data of the diffusion experiment tabulated in Table S1 in Supporting Information S1.

The transport parameters obtained for the three SF-OPA samples from Mt. Terri are given in Table 2. The accessible porosities vary between 0.17 and 0.20. The obtained accessible porosity of sample BAD-1 is slightly higher than the one of BAD-3 by a factor of 1.2. The main difference between the BAD-1 and BAD-3 rock samples lies in their heterogeneous microstructures (cf. Figure 5). A similar trend was observed by Houben (2013), in which the porosities of different OPA facies were characterized by MIP, considering that MIP measures the connected porosity down to a pore throat size of 3 nm.

The effective diffusion coefficients listed in Table 2 for HTO diffusion in samples BAD-1, BAD-2, and BAD-3 are $D_e = 9.0 \times 10^{-11}$, 8.5×10^{-11}, and 7.2×10^{-11} m²/s, respectively. Their relative error ε_{D_e/D_0} is 0.226 ($D_0 = 2 \times 10^{-9}$ m²/s) as the volume of the sample is 7,070 mm³. This variability also indicates a high heterogeneity of the pore space geometry in SF-OPA (see Figures 11a and 11b). Besides, an exponent of $n = 1.9$ in Archie's law was derived for HTO diffusion in SF-OPA by fitting with the experimental data in Table 2.
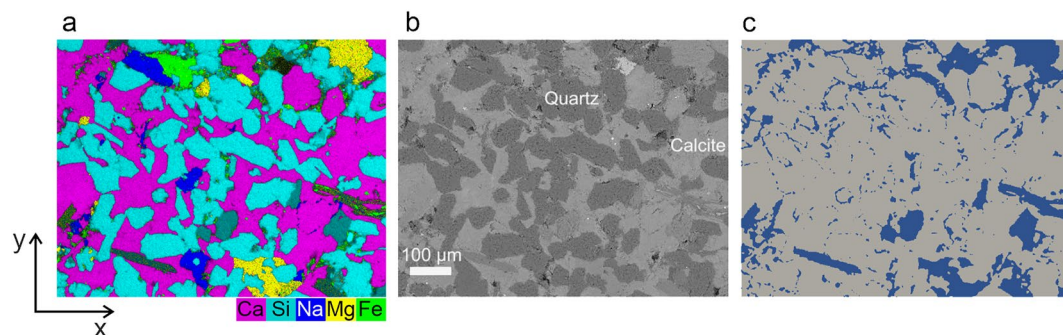

Figure 11. (a) SEM-EDX elemental map in false colors overlaid on the electron image of a mixture of clay, sand, and calcite crystals in sandy facies of OPA from the same drill core as BAD 1-3. (b) Backscattered electron image from the area (a). (c) Segmented clay minerals (blue color) and non-clay mineral components (gray color) derived from the treatment of image (a) by Image J software. The fraction of clay minerals is 19.3%.
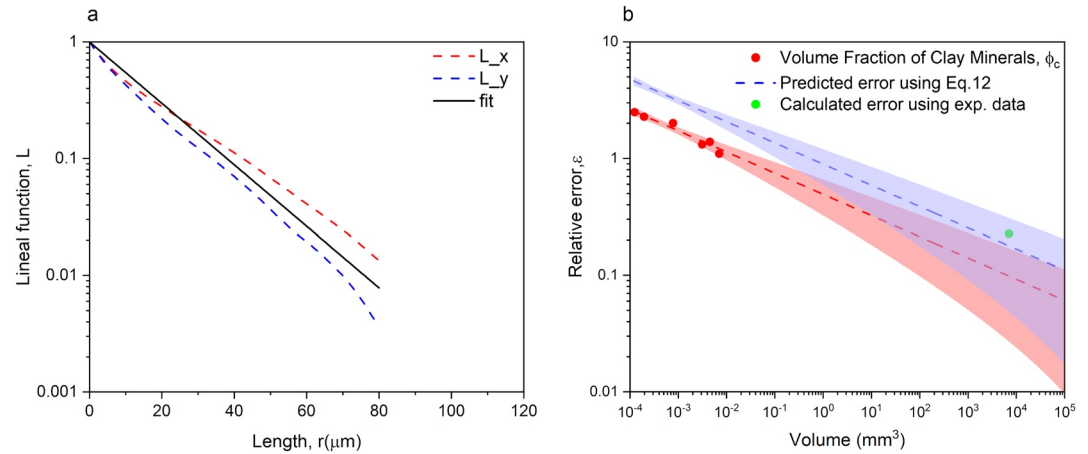
Figure 12. (a) The lineal-path function $L^c(r)$ of clay minerals versus the distance r along with x and y directions and the fit curve based on Equation 6 with $m = 2.3$ and $R_c = 199\ \mu$m (red line). (b) The relative errors of volume fraction of clay minerals and diffusivity as a function of volume from our predictions. Red points are the relative errors of volume fraction of clay minerals $\varepsilon_{VA}(V)$ and the red dashed line is the calibration curve. The green point and the blue dashed line are the relative errors of diffusivity in sandy facies of OPA from the triated water diffusion experiments and our prediction by Equation 12, respectively. Red and blue regions are 90% confidence regions for the corresponding fitting lines.

To calculate the lineal-path function of a selected region, an SEM-EDX elemental map of a mixture of clay, sand, and calcite crystals in SF-OPA (Figure 11a) is used to segment clay and non-clay minerals (Figure 11c). Based on the composition of clay and non-clay minerals in Table S2 in Supporting Information S1 (Gaucher et al., 2003), the pink (Ca), light blue (Si), blue (Na), and green (Fe) colors are treated as the non-clay minerals; the yellow (Mg), gray-blue (illite/smectite), and other mixed colors are assigned to clay minerals. Figure 11c illustrates the distribution of clay mineral aggregates and non-clay minerals derived by using the ImageJ software. Note that the blue color area in Figure 11c might contain other sheet silicates such as micas. Nevertheless, the clay minerals in the blue color area are still the major components. Therefore, containing such other sheet silicates will not significantly change the lineal-path curves and the corresponding characteristic length. The relationship between REVand REA for porosity in SF-OPA was derived using the method described in Section 2.4. Figure 12a shows the calculated lineal-path functions along x and y directions based on the segmented image (Figure 11c) using Equation 5. After fitting Equation 6 with $m = 2.3$ to the lineal-path functions in both x and y directions, we can determine $R_c = 199\ \mu$m. Besides, the segmented image was split into 4×3 sub-regions to calculate the relative errors of clay fraction $\varepsilon_{VA}(V)$ (red points in Figure 12b). The red dashed line is the corresponding fitting curve ($R^2 = 0.95$) on the log-log scale. Hence, based on $\varepsilon_{D_e/D_0} = n \times \varepsilon_{VA}$ (cf. Equation 12), we can predict the relative error of the effective diffusivity (blue dashed line in Figure 12b). From the through-diffusion experiments, the relative error of HTO effective diffusivities in SF-OPA is 0.226 as the sample volume is $7.07\ \text{cm}^3$ ($\varepsilon_{D_e/D_0}\left(7.07\ \text{cm}^3\right) = 0.226$, green point in Figure 12b), which is covered in our theoretical prediction (blue dashed line with 90% confidence interval in Figure 12b). The relative error at the same volume predicted by our model ranges from 0.06 to 0.3. Through our prediction curve in Figure 12b, the REV for diffusivity in SF-OPA should be around $100\ \text{cm}^3$ by using a rigorous $\varepsilon_{D_e/D_0} = 0.1$. Considering the large heterogeneity of clay rocks, a rough predefined relative error for REV $\varepsilon_{D_e/D_0} = 0.1 \sim 0.4$ is adopted, and the corresponding REV for diffusivity in SF-OPA will decrease to about $1\ \text{cm}^3$. The large range of the predicted relative error is caused by the limited experimental data (cf. red points in Figure 12b). More data would result in a tendency of narrowing the spreading of the 90% confidence region (cf. red and blue regions in Figure 12b). Possible corrections and improvements will be the subject of future investigations.

4. Summary and Conclusions

In this study, we present a comprehensive analysis of heterogeneities for both porosity and diffusivity in clay rocks by using the classical sampling theory and pore-scale simulations. REA and REV are critical to quantify the effective diffusivity in RT models. Based on synthetic digital clay rocks, our results reveal that the REV for

diffusivity is larger than the REV for porosity. This is a generalizable result if porous materials have complex pore network geometries (Grathwohl, 1998). Consequently, the discrepancy between the REV for transport properties such as effective diffusivity and the REV for porosity becomes larger in a porous material with a lower connectivity and a larger tortuosity. Therefore, in numerical simulations of diffusive transport at the continuum scale, the bulk parameters should be defined over a diffusion-based REV rather than a porosity-based REV, especially in very heterogeneous porous materials. To calculate the diffusion-based REV in clay rocks, this study has developed quantitative relationships between the REA for porosity, the REV for porosity, and the REV for diffusivity. A quantitative method was developed to correlate the REA for porosity with the REV for porosity via the lineal-path function and the characteristic length based on six different digital microstructures. Our results show that the REVs for porosity and diffusivity can be correlated via Archie's law. The predicted REV for diffusivity by our proposed correlation generally has a good agreement with the one determined by the calculated diffusivities. This demonstrates that the proposed correlation can predict the REV for diffusivity via the volumetric porosities. In such a way, the REV for diffusivity can be determined by the developed correlations by analyzing two-dimensional microstructures of clay rocks. The applicability of our approach for clay rocks was validated by the experimental data on the through-diffusion of HTO in samples of SF-OPA. From the predictions, the REV for HTO diffusivity in SF-OPA is around $1\,\mathrm{cm}^3$ by using an acceptable rough relative error $\varepsilon_{D_e/D_0} = 0.1 \sim 0.4$. Our approach provides a promising way to determine diffusion-based REVs using the developed correlations from two-dimensional sections of SF-OPA. Consequently, the computational cost can be significantly reduced compared with the classical calculations of REV for diffusivity. This study provides a critical understanding of solute and radionuclide migration in heterogeneous SF-OPA within the context of deep geological disposal of nuclear waste. Though this study only considers the diffusion process, the developed relationships can be expanded to other transport processes such as fluidic permeability and electrical conductivity in heterogeneous porous media.

Data Availability Statement

The data are available at https://doi.org/10.5281/zenodo.7014529.

References

Appelo, C. A. J., Van Loon, L. R., & Wersin, P. (2010). Multicomponent diffusion of a suite of tracers (HTO, Cl, Br, I, Na, Sr, Cs) in a single sample of Opalinus Clay. *Geochimica et Cosmochimica Acta*, *74*(4), 1201–1219. https://doi.org/10.1016/j.gca.2009.11.013

Bear, J., & Bachmat, Y. (1984). Transport phenomena in porous media—Basic equations. In J. Bear (Ed.), *Fundamentals of transport phenomena in porous media* (pp. 3–61). Springer.

Beckingham, L. E., Peters, C. A., Um, W., Jones, K. W., & Lindquist, W. B. (2013). 2D and 3D imaging resolution trade-offs in quantifying pore throats for prediction of permeability. *Advances in Water Resources*, *62*, 1–12. https://doi.org/10.1016/j.advwatres.2013.08.010

Bernabé, Y., Li, M., & Maineult, A. (2010). Permeability and pore connectivity: A new model based on network simulations. *Journal of Geophysical Research*, *115*(B10), B10203. https://doi.org/10.1029/2010jb007444

Bernabé, Y., Li, M., Tang, Y.-B., & Evans, B. (2016). Pore space connectivity and the transport properties of rocks. *Oil & Gas Science and Technology—Revue d'IFP Energies nouvelles*, *71*(4), 50. https://doi.org/10.2516/ogst/2015037

Bernabé, Y., Zamora, M., Li, M., Maineult, A., & Tang, Y. B. (2011). Pore connectivity, permeability, and electrical formation factor: A new model and comparison to experimental data. *Journal of Geophysical Research*, *116*(B11), B11204. https://doi.org/10.1029/2011jb008543

Bollermann, T., Yuan, T., Kulenkampff, J., Stumpf, T., & Fischer, C. (2022). Pore network and flow field analysis towards improved predictability of diffusive transport in argillaceous host rocks. *Chemical Geology*, *606*, 120997. https://doi.org/10.1016/j.chemgeo.2022.120997

Bossart, P., & Thurry, M. (2008). Swiss Geological Survey, Wabern, Switzerland. Mont Terri Rock Laboratory. Project, programme 1996 to 2007 and results. Retrieved from no. 3. Swiss Geological Survey.

Boving, T. B., & Grathwohl, P. (2001). Tracer diffusion coefficients in sedimentary rocks: Correlation to porosity and hydraulic conductivity. *Journal of Contaminant Hydrology*, *53*(1–2), 85–100. https://doi.org/10.1016/s0169-7722(01)00138-3

Chen, L., Kang, Q., Dai, Z., Viswanathan, H. S., & Tao, W. (2015). Permeability prediction of shale matrix reconstructed using the elementary building block model. *Fuel*, *160*, 346–356. https://doi.org/10.1016/j.fuel.2015.07.070

Cosenza, P., Giot, R., Giraud, A., & Hedan, S. (2021). A fractional differential scheme for the effective transport properties of multiscale reactive porous media: Applications to clayey geomaterials. *International Journal for Numerical and Analytical Methods in Geomechanics*, *45*(14), 2130–2154. https://doi.org/10.1002/nag.3259

Cosenza, P., Prêt, D., Fauchille, A.-L., & Hedan, S. (2019). Representative elementary area of shale at the mesoscopic scale. *International Journal of Coal Geology*, *216*, 103316. https://doi.org/10.1016/j.coal.2019.103316

dos Santos, M. A. F., & Menon Junior, L. (2020). Log-normal superstatistics for Brownian particles in a heterogeneous environment. *Physics*, *2*(4), 571–586. https://doi.org/10.3390/physics2040032

Fernandes, J. S., Appoloni, C. R., & Fernandes, C. P. (2012). Determination of the representative elementary volume for the study of sandstones and siltstones by X-Ray microtomography. *Materials Research*, *15*(4), 662–670. https://doi.org/10.1590/s1516-14392012005000081

Gaucher, E., Fernández, A., & Waber, H. (2003). Rock and mineral characterisation of the Opalinus Clay formation. Mont Terri Project–Geochemistry of water in the Opalinus Clay formation at the Mont Terri Rock Laboratory. *Reports of the Federal Office for Water and Geology (FOWG), Geology Series*, *5*, 281–303.

Glaus, M. A., Aertsens, M., Appelo, C. A. J., Kupcik, T., Maes, N., Van Laer, L., & Van Loon, L. R. (2015). Cation diffusion in the electrical double layer enhances the mass transfer rates for Sr^{2+}, Co^{2+} and Zn^{2+} in compacted illite. *Geochimica et Cosmochimica Acta*, *165*, 376–388. https://doi.org/10.1016/j.gca.2015.06.014

Glaus, M. A., Baeyens, B., Bradbury, M. H., Jakob, A., Van Loon, L., & Yaroshchuk, A. (2007). Diffusion of ^{22}Na and ^{85}Sr in Montmorillonite: Evidence of Interlayer diffusion being the dominant pathway at high compaction. *Environmental Science and Technology*, *41*(2), 478–485. https://doi.org/10.1021/es061908d

Grathwohl, P. (1998). *Diffusion in natural porous media: Contaminant transport, sorption/desorption and dissolution kinetics*. Springer Science+Business Media.

Hornung, U. (1997). *Homogenization and porous media*. Springer.

Houben, M. E. (2013). *In situ characterization of the microstructure and porosity of Opalinus clay (Mont Terri rock laboratory, Switzerland). (Ph.D. Dissertation)*. RWTH Aachen University.

Houben, M. E., Desbois, G., & Urai, J. L. (2014). A comparative study of representative 2D microstructures in Shaly and Sandy facies of Opalinus Clay (Mont Terri, Switzerland) inferred form BIB-SEM and MIP methods. *Marine and Petroleum Geology*, *49*, 143–161. https://doi.org/10.1016/j.marpetgeo.2013.10.009

Joseph, C., Van Loon, L. R., Jakob, A., Steudtner, R., Schmeide, K., Sachs, S., & Bernhard, G. (2013). Diffusion of U(VI) in Opalinus clay: Influence of temperature and humic acid. *Geochimica et Cosmochimica Acta*, *109*, 74–89. https://doi.org/10.1016/j.gca.2013.01.027

Jülich Supercomputing Centre. (2018). Data centric and booster modules implementing the modular supercomputing architecture at Jülich Supercomputing Centre. *Journal of large-scale research facilities*, *7*, A182. https://doi.org/10.17815/jlsrf-7-182

Kanit, T., Forest, S., Galliet, I., Mounoury, V., & Jeulin, D. (2003). Determination of the size of the representative volume element for random composites: Statistical and numerical approach. *International Journal of Solids and Structures*, *40*(13–14), 3647–3679. https://doi.org/10.1016/s0020-7683(03)00143-4

Keller, L. M., Hilger, A., & Manke, I. (2015). Impact of sand content on solute diffusion in Opalinus Clay. *Applied Clay Science*, *112–113*, 134–142. https://doi.org/10.1016/j.clay.2015.04.009

Keller, L. M., & Holzer, L. (2018). Image-based upscaling of permeability in Opalinus clay. *Journal of Geophysical Research: Solid Earth*, *123*(1), 285–295. https://doi.org/10.1002/2017jb014717

Keller, L. M., Holzer, L., Schuetz, P., & Gasser, P. (2013). Pore space relevant for gas permeability in Opalinus Clay: Statistical analysis of homogeneity, percolation, and representative volume element. *Journal of Geophysical Research: Solid Earth*, *118*(6), 2799–2812. https://doi.org/10.1002/jgrb.50228

Kim, D.-H., Kim, D.-K., Zhou, K., Park, S., Kwon, Y., Jeong, M. G., et al. (2017). Single particle tracking-based reaction progress kinetic analysis reveals a series of molecular mechanisms of cetuximab-induced EGFR processes in a single living cell. *Chemical Science*, *8*(7), 4823–4832. https://doi.org/10.1039/C7SC01159H

Kulenkampff, J., Gründig, M., Zakhnini, A., Gerasch, R., & Lippmann-Pipke, J. (2015). Process tomography of diffusion, using PET, to evaluate anisotropy and heterogeneity. *Clay Minerals*, *50*(3), 369–375. https://doi.org/10.1180/claymin.2015.050.3.09

Leupin, O. X., Van Loon, L. R., Gimmi, T., Wersin, P., & Soler, J. M. (2017). Exploring diffusion and sorption processes at the Mont Terri rock laboratory (Switzerland): Lessons learned from 20 years of field research. *Swiss Journal of Geosciences*, *110*(1), 391–403. https://doi.org/10.1007/s00015-016-0254-z

Lu, B., & Torquato, S. (1992). Lineal-path function for random heterogeneous materials. *Phys Rev A*, *45*(2), 922–929. https://doi.org/10.1103/physreva.45.922

Navarre-Sitchler, A., Steefel, C. I., Yang, L., Tomutsa, L., & Brantley, S. L. (2009). Evolution of porosity and diffusivity associated with chemical weathering of a basalt clast. *Journal of Geophysical Research*, *114*(F2), F02016. https://doi.org/10.1029/2008jf001060

Oh, B. H., & Jang, S. Y. (2004). Prediction of diffusivity of concrete based on simple analytic equations. *Cement and Concrete Research*, *34*(3), 463–480. https://doi.org/10.1016/j.cemconres.2003.08.026

Pearson, F. J. (1998). *Opalinus clay experimental water: A1 Type, Version 980318. PSI Internal report TM-44-98-07*. Retrieved from Paul Scherrer Institut, Villigen PSI, Switzerland.

Peters, C. A. (2009). Accessibilities of reactive minerals in consolidated sedimentary rock: An imaging study of three sandstones. *Chemical Geology*, *265*(1–2), 198–208. https://doi.org/10.1016/j.chemgeo.2008.11.014

Philipp, T., Amann-Hildenbrand, A., Laurich, B., Desbois, G., Littke, R., & Urai, J. L. (2017). The effect of microstructural heterogeneity on pore size distribution and permeability in Opalinus Clay (Mont Terri, Switzerland): Insights from an integrated study of laboratory fluid flow and pore morphology from BIB-SEM images. *Geological Society, London, Special Publications*, *454*(1), 85–106. https://doi.org/10.1144/sp454.3

Pret, D., Sammartino, S., Beaufort, D., Fialin, M., Sardini, P., Cosenza, P., & Meunier, A. (2010). A new method for quantitative petrography based on image processing of chemical element maps: Part II. Semi-Quantitative porosity maps superimposed on mineral maps. *American Mineralogist*, *95*(10), 1389–1398. https://doi.org/10.2138/am.2010.3433

Robinet, J.-C., Sardini, P., Coelho, D., Parneix, J.-C., Prêt, D., Sammartino, S., et al. (2012). Effects of mineral distribution at mesoscopic scale on solute diffusion in a clay-rich rock: Example of the Callovo-Oxfordian mudstone (Bure, France). *Water Resources Research*, *48*(5). https://doi.org/10.1029/2011wr011352

Robinet, J. C., Sardini, P., Siitari-Kauppi, M., Prêt, D., & Yven, B. (2015). Upscaling the porosity of the Callovo-Oxfordian mudstone from the pore scale to the formation scale; insights from the 3H-PMMA autoradiography technique and SEM BSE imaging. *Sedimentary Geology*, *321*, 1–10. https://doi.org/10.1016/j.sedgeo.2015.02.007

Soler, J. M., Landa, J., Havlova, V., Tachi, Y., Ebina, T., Sardini, P., et al. (2015). Comparative modeling of an in situ diffusion experiment in granite at the Grimsel Test Site. *Journal of Contaminant Hydrology*, *179*, 89–101. https://doi.org/10.1016/j.jconhyd.2015.06.002

Van Loon, L. R., Baeyens, B., & Bradbury, M. H. (2005). Diffusion and retention of sodium and strontium in Opalinus clay: Comparison of sorption data from diffusion and batch sorption measurements, and geochemical calculations. *Applied Geochemistry*, *20*(12), 2351–2363. https://doi.org/10.1016/j.apgeochem.2005.08.008

Van Loon, L. R., & Jakob, A. (2005). Evidence for a Second transport porosity for the diffusion of tritiated water (HTO) in a sedimentary rock (Opalinus Clay—OPA): Application of through- and out-diffusion techniques. *Transport in Porous Media*, *61*(2), 193–214. https://doi.org/10.1007/s11242-004-7464-y

Van Loon, L. R., Soler, J. M., & Bradbury, M. H. (2003). Diffusion of HTO, 36Cl− and 125I− in Opalinus Clay samples from Mont Terri. *Journal of Contaminant Hydrology*, *61*(1–4), 73–83. https://doi.org/10.1016/s0169-7722(02)00114-6

Van Loon, L. R., Wersin, P., Soler, J. M., Eikenberg, J., Gimmi, T., Hernan, P., et al. (2004). In-situ diffusion of HTO, ^{22}Na+, Cs+ and I− in Opalinus Clay at the Mont Terri underground rock laboratory. *Radiochimica Acta*, *92*(9–11), 757–763. https://doi.org/10.1524/ract.92.9.757.54988

Wang, M., Wang, J., Pan, N., & Chen, S. (2007). Mesoscopic predictions of the effective thermal conductivity for microscale random porous media. *Physical Review E*, *75*(3 Pt 2), 036702. https://doi.org/10.1103/PhysRevE.75.036702

Wang, Z., Jin, X., Wang, X., Sun, L., & Wang, M. (2016). Pore-scale geometry effects on gas permeability in shale. *Journal of Natural Gas Science and Engineering*, *34*, 948–957. https://doi.org/10.1016/j.jngse.2016.07.057

Wersin, P., Soler, J. M., Van Loon, L., Eikenberg, J., Baeyens, B., Grolimund, D., et al. (2008). Diffusion of HTO, Br$^-$, I$^-$, Cs$^+$, ^{85}Sr^{2+} and ^{60}Co^{2+} in a clay formation: Results and modelling from an in situ experiment in Opalinus Clay. *Applied Geochemistry*, *23*(4), 678–691. https://doi.org/10.1016/j.apgeochem.2007.11.004

Wigger, C., & Van Loon, L. (2018). Effect of the pore water composition on the diffusive anion transport in argillaceous, low permeability sedimentary rocks. *Journal of Contaminant Hydrology*, *213*, 40–48. https://doi.org/10.1016/j.jconhyd.2018.05.001

Yang, Y., Patel, R. A., Churakov, S. V., Prasianakis, N. I., Kosakowski, G., & Wang, M. (2019). Multiscale modeling of ion diffusion in cement paste: Electrical double layer effects. *Cement and Concrete Composites*, *96*, 55–65. https://doi.org/10.1016/j.cemconcomp.2018.11.008

Yang, Y., & Wang, M. (2018). Pore-scale modeling of chloride ion diffusion in cement microstructures. *Cement and Concrete Composites*, *85*, 92–104. https://doi.org/10.1016/j.cemconcomp.2017.09.014

Yeong, C. L. Y., & Torquato, S. (1998). Reconstructing random media. *Physical Review E*, *57*(1), 495–506. https://doi.org/10.1103/physreve.57.495

Yio, M. H. N., Wong, H. S., & Buenfeld, N. R. (2017). Representative elementary volume (REV) of cementitious materials from three-dimensional pore structure analysis. *Cement and Concrete Research*, *102*, 187–202. https://doi.org/10.1016/j.cemconres.2017.09.012

Yuan, T., & Fischer, C. (2021). Effective diffusivity prediction of radionuclides in clay formations using an integrated upscaling workflow. *Transport in Porous Media*, *138*(2), 245–264. https://doi.org/10.1007/s11242-021-01596-0

Yuan, T., & Fischer, C. (2022). The influence of sedimentary and diagenetic heterogeneity on the radionuclide diffusion in the sandy facies of the Opalinus Clay at the core scale. *Applied Geochemistry*, *146*, 105478. https://doi.org/10.1016/j.apgeochem.2022.105478

Yuan, T., & Qin, G. (2020). Numerical investigation of wormhole formation during matrix acidizing of carbonate rocks by coupling Stokes-Brinkman equation with reactive transport model under radial flow conditions. In *Paper presented at the SPE international conference and exhibition on formation damage control, Louisiana*.

Yuan, T., Wei, C., Zhang, C.-S., & Qin, G. (2019). A numerical simulator for modeling the coupling processes of subsurface fluid flow and reactive transport processes in fractured carbonate rocks. *Water*, *11*(10), 1957. https://doi.org/10.3390/w11101957